AD-A078 222 WESTINGHOUSE RESEARCH AND DEVELOPMENT CENTER PITTSBU--ETC F/G 13/8
INVESTIGATION OF WELD POOL STRUCTURE AND PROPERTY CONTROL IN PU--ETC(U)
NOV 79 G M ECER , G G LESSMANN , H D BRODY N00014-77-C-0596
UNCLASSIFIED 79-9D4-PULSE-R1 NL

| OF |
ADA
078222

END
DATE
FILMED
1 -80
DDC

INVESTIGATION OF WELD POOL STRUCTURE AND PROPERTY CONTROL IN PULSED ARC WELDING

G. M. Ecer, Principal Investigator
G. G. Lessmann, Project Manager
Westinghouse R&D Center

H. D. Brody, Project Director
University of Pittsburgh

Annual Progress Report (September 15, 1978 - September 14, 1979)
ONR Contract N00014-77-C0596

November 9, 1979

Office of Naval Research
800 North Quincy Road
Arlington, VA 22217
Scientific Officer: Bruce A. MacDonald (Code 471)

Westinghouse R&D Center
1310 Beulah Road
Pittsburgh, Pennsylvania 15235

INVESTIGATION OF WELD POOL STRUCTURE AND PROPERTY CONTROL IN PULSED ARC WELDING

G. M. Ecer, Principal Investigator
G. G. Lessmann, Project Manager
Westinghouse R&D Center

H. D. Brody, Project Director
University of Pittsburgh

Annual Progress Report (September 15, 1978 - September 14, 1979)
ONR Contract N00014-77-C0596

November 9, 1979

Office of Naval Research
800 North Quincy Road
Arlington, VA 22217
Scientific Officer: Bruce A. MacDonald (Code 471)

Westinghouse R&D Center
1310 Beulah Road
Pittsburgh, Pennsylvania 15235

SECURITY CLASSIFICATION OF THIS PAGE (When Data Entered)

REPORT DOCUMENTATION PAGE

READ INSTRUCTIONS BEFORE COMPLETING FORM

1. REPORT NUMBER

2. GOVT ACCESSION NO.

3. RECIPIENT'S CATALOG NUMBER

4. TITLE (and Subtitle)

(6) INVESTIGATION OF WELD POOL STRUCTURE AND PROPERTY CONTROL IN PULSED ARC WELDING.

5. TYPE OF REPORT & PERIOD COVERED
Technical Report
Sept. 15, 1978 to Sept. 14, 1979

6. PERFORMING ORG. REPORT NUMBER

7. AUTHOR(s)

(10) G. M. Ecer, G. G. Lessmann, H. D. Brody

8. CONTRACT OR GRANT NUMBER(s)

N00014-77-C0596

9. PERFORMING ORGANIZATION NAME AND ADDRESS

Westinghouse R&D Center, Pittsburgh, PA 15235
University of Pgh., MME Dept., Pittsburgh, PA 15213

10. PROGRAM ELEMENT, PROJECT, TASK AREA & WORK UNIT NUMBERS

(15) N00014-77-C-0596

11. CONTROLLING OFFICE NAME AND ADDRESS

Office of Naval Research
Metallurgy and Ceramics Program
Arlington, VA 22217

(11)

12. REPORT DATE
9 November 1979

13. NUMBER OF PAGES
55

14. MONITORING AGENCY NAME & ADDRESS (if different from Controlling Office)

Dr. B. A. MacDonald, Metallurgy Division
Office of Naval Research, Code 471
Department of the Navy
Arlington, VA 22217

15. SECURITY CLASS. (of this report)
Unclassified

15a. DECLASSIFICATION/DOWNGRADING SCHEDULE

16. DISTRIBUTION STATEMENT (of this Report)

(12) 57

This document has been approved for public release and sale; its distribution is unlimited.

17. DISTRIBUTION STATEMENT (of the abstract entered in Block 20, if different from Report)

Approved for public release; distribution unlimited.

(9) Annual progress rept. 15 Sep 78 - 14 Sep 79

18. SUPPLEMENTARY NOTES

(14) 79-9D4-PULSE-R1

19. KEY WORDS (Continue on reverse side if necessary and identify by block number)

Structure, Solidification, Pulsed, Arcs, Welding, Control, Heat, Flow, Modeling, Computers, Ripple.

20. ABSTRACT (Continue on reverse side if necessary and identify by block number)

Full penetration pulsed current gas tungsten arc welds on Fe-26Ni alloy sheets were dimensionally and structurally analyzed. Weld pool kinetics and weld surface ripple formation were studied using high speed motion pictures, conventional and scanning electron metallography, and x-ray dispersive analysis. The two dimensional heat flow computer model developed during the last year was modified to reflect more realistic convective flow in the weld pool, anode size and atmospheric heat loss. Work on thick plate welds and the

DD FORM 1 JAN 73 1473 EDITION OF 1 NOV 65 IS OBSOLETE
S/N 0102-LF-014-6601

SECURITY CLASSIFICATION OF THIS PAGE (When Data Entered)

20. ABSTRACT (cont.)

computational model for 3D heat flow and solute segregation under pulsing were initiated. Some degree of structural control in the weld fusion zone of full penetration welds was found to be feasible. A mechanism for the formation of weld surface ripples and a technique of estimating local solid growth rates from the ripples were proposed.

TABLE OF CONTENTS

79-9D4-PULSE-R1 November 9, 1979

INVESTIGATION OF WELD POOL STRUCTURE AND PROPERTY CONTROL IN PULSED ARC WELDING

G. M. Ecer, Principal Investigator
G. G. Lessmann, Project Manager
Westinghouse R&D Center
Pittsburgh, PA 15235

H. D. Brody, Project Director
University of Pittsburgh
Pittsburgh, PA

ABSTRACT

Full penetration pulsed current gas tungsten arc welds on Fe-26Ni alloy sheets were dimensionally and structurally analyzed. Weld pool kinetics and weld surface ripple formation were studied using high speed motion pictures, conventional and scanning electron metallography, and x-ray dispersive analysis. The two dimensional heat flow computer model developed during the last year was modified to reflect more realistic convective flow in the weld pool, anode size,and atmospheric heat loss. Work on thick plate welds and the computational model for 3D heat flow and solute segregation under pulsing were initiated. Some degree of structural control in the weld fusion zone of full penetration welds was found to be feasible. A mechanism for the formation of weld surface ripples and a technique of estimating local solid growth rates from the ripples were proposed.

FORWARD

This progress report was prepared by the Westinghouse Electric Corporation in collaboration with the University of Pittsburgh, under Office of Naval Research Contract N00014-77-C0596, "Investigation of Weld Pool Structure and Property Control in Pulsed Arc Welding". The program was administered under the technical direction of the Office of Naval Research, Department of the Navy, Arlington, VA, with Dr. Bruce A. MacDonald (Code 471) serving as the ONR Scientific Officer in charge of inspection and acceptance of the program.

The project work is being carried out by the Westinghouse Electric Corporation with the University of Pittsburgh, Metallurgical and Materials Engineering Department acting as a subcontractor.

The Westinghouse part of the program is managed by Mr. G. G. Lessmann, Manager of Metals Joining and Metals Processing, and technically directed by Dr. G. M. Ecer. Significant contributions were also made by T. Mullen (x-ray dispersive analysis), R. Berrier (metallography) and K. Grande (typing).

The University of Pittsburgh part of the program is managed and technically directed by Dr. H. D. Brody, Professor of Metallurgical and Materials Engineering. Mr. M. Vassilaros prepared the initial computer model as part of a course project. Mr. Tri Dinh contributed to modifications of the program and performed the correlations with experiment. Mr. A. Gokhale was involved in cinematographic analysis of weld pool kinetics.

1.0 INTRODUCTION

Pulsed current arc welding, unlike steady current welding, is capable of producing periodically changing cooling rates along the weld seam, thus affecting the primary and secondary solidification patterns of the weld pool. The mode of solidification, on the other hand, substantially determines the weld metal properties, by influencing grain size and orientation, phases precipitated as well as the segregation processes. The wide range of solidification rates which are possible with pulsed current arc welding processes make them highly desirable methods for controlling weld properties. Development of methods of weld structure control can produce significant improvements in weldment properties and reliability with considerable economic benefits.

The added flexibility of the pulsed current process, relative to weld structural control, results from the four new process variables emerging from the cycling of the arc current between high (i_p) and low or background (i_b) current levels with their corresponding durations, t_p and t_b, as defined in Figure 1. Further flexibility may be designed into the current waveform by increasing its complexity to obtain, for example, pre or post weld heat treatment of a weld spot formed under the high current arc, or high frequency modulation of the current for penetration control. In its simplest form, the square current waveform, as seen in Figure 1, allows higher energy rate welding for a lower heat input weld. Thus, a higher portion of the heat absorbed by the weldment is used for the formation of the weld fusion zone.

The overall objective of the present program is to control weldment properties by establishing relationships between the properties and pulsed current welding process variables. Under the ONR Contract N00014-77-C-0596, work began early in 1978, with the University of Pittsburgh acting as a subcontractor to Westinghouse. The first year's effort was focused on the development of a predictive mathematical model of pulsed arc welding of thin sheets (two-dimensional heat flow) and establishing the experimental techniques to develop physical data to

correlate process variables to weld solidification structure. In 1979, the two dimensional model modifications, weld pool kinetics, 3-D welds and solute segregation were the areas of concentration. This progress report summarizes the 1979 work.

2.0 METHODOLOGY

2.1 Analytical Study

A dual approach, experimental and analytical, was adopted to generate data needed in the development of a model correlating weld process parameters to the solidification variables. The analytical approach provided for the development of a mathematical model which would simulate, in the first phase of the study, heat flow conditions encountered in pulsed arc welding of thin sheets. The model developed, as most similar models, uses the method of finite differences to describe heat flow in two directions from a continuous or pulsing heat source moving with constant speed on a plane with known thermal properties. The model utilizes a matrix with approximately 500 elements. It can be used with and without heat losses to the environment and it can take into account convection effects in the liquid phase, latent heat of fusion, temperature dependent conductivity, heat capacity and density of the base metal. In simulations reported here, all elements have been considered to be at 25°C, when the run starts; although preheat may be simulated as well. Computation is stopped when the temperature has stabilized with respect to time. The model is described in more detail elsewhere[1] and in Section 4.0.

In summary, the model uses a digital computer to solve a large number of relatively simple heat flow equations. The equations describe the temperature change of a small volume of metal experiencing heat flow to or from the neighboring volume elements. Each element is described by a single temperature of an assumed concentrated mass at the element's center. The temperature differences between all the adjacent elements are used to compute the heat flow between elements and thus predict the temperatures after a given time interval. The use of small time intervals minimizes any errors in predicting the temperatures.

Initial tests[2,3] of the model included a comparison of the model predictions with those by Adams'[4] equation for temperature profiles of a continuous current weld, and those by Wells'[5] equation for the maximum bead width for continuous welds. In both cases, the predictions were within 10% of each other. Using experimentally estimated heat transfer efficiency (μ)* of the process, and material properties, i.e., thermal conductivity, density, specific heat, estimated from data disclosed in literature, the pulsed arc welding model for the two-dimensional heat flow welds of Fe-26Ni alloy predicted temperature profiles and temperature gradients with acceptable accuracy, i.e., within 15% of experimental, and somewhat smaller bead widths in the early tests of the model.

2.2 Experimental

Table 2 lists all the pulsed current gas tungsten arc welds done on the Fe-26Ni alloy. Welds in the F through L series were intended to simulate two dimensional heat flow conditions, i.e., thin sheet welds, and have been described in detail earlier[2]. Series M through S were performed this year mainly to simulate welding under three dimensional heat extraction conditions. Although the Fe-26Ni alloy plates were thicker than 0.08 cm in these latter series, the method of preparation, described fully earlier[2], remained the same. Similarly, weld set-up, shown in Figure 2, electrode, gas shielding and power supply characteristics were also unchanged. These variables were selected to provide the same arc current-arc voltage relation by keeping the arc atmosphere, electrode geometry and arc gap constant. Weld set-up, once again, minimized heat loss to the weld fixture and assured arc stability by providing a symmetrical current path to the ground.

A second set of welds, "T" series, listed in Table 3, were made on a 30 mm thick section of a Fe-36Ni alloy slab in as hot forged condition. The weld process related controls were identical to those used for the welds on the Fe-26Ni alloy.

---

*All symbols are defined in Table 1.

A cold finished carbon steel plate (nominal chemistry: Fe - 0.13 max C - 0.85 Mn - 0.10 P - 0.30 S) was used for an initial experimentation to assess differences in the manner sulfur segregates under steady current and pulsed current welding conditions. The four welds made are listed in Table 4. Sulfur prints of these welds were made after belt polishing the weld plate surface. Attempts to weld over localized concentrations of sulfur (sulfur placed in drilled small holes in the weld plate) were unsuccessful, as the sulfur quickly evaporated under the welding arc. The latter experiments, if they had succeeded, were to determine the effect of pulsing on the transport of a localized solute concentration along the weld seam.

A number of welds listed in Table 2 were optically and electron metallographically examined for structural variations and solidification morphology. High speed (1000 frames per second) cinematography was utilized for analysis of weld pool kinetics in the following welds: F3,G1,G5,J4,J6,J7,H8,L1,M1,M3, and M4. These welds were also examined to determine patterns of weld surface ripple formation. Chemistry differences at and around the ripples on sample G5 were determined by energy dispersive x-ray analysis using a 1-1.5 μm diameter electron beam. Approximate percentages of the desired elements were computer calculated.

3.0 EXPERIMENTAL RESULTS AND DISCUSSION

3.1 Thin Sheet Welds

3.1.1 Weld Bead Pool Shapes

Weld pool shape can be a reflection of the weld mechanical properties as it is closely tied to the amount and mode of segregation resulting from solidification. Solid phase growth occurs in the direction of the maximum negative thermal gradient which is perpendicular to the solid-liquid interface at all points of the weld pool. Since growing solid tends to reject solute, the liquid ahead of the growing grains becomes enriched in solutes which lower the melting point. In the absence of weld pool fluid flow that can completely redistribute the rejected solute, a dangerously high concentration of melting point lowering elements at the centerline may lead to hot-cracking. Such a situation is created when the welding process parameters chosen promote an elongated, tear-drop shaped weld pool where grains grow directly onto each other from both sides meeting at the weld thermal centerline. On the otherhand an elliptical shaped pool may eliminate centerline segregation and reduce overall severity of segregation. Not only the grains would follow the elliptical pool, changing direction continuously, but the growth front would be nearer the arc, thus, may come under the influence of fluid flow caused by Lorentz's force. The regions of greatest solute enrichment, in this case, would be the grain boundaries. The weld metal failure under stress, then, would tend to occur along the grain boundaries.

Cold cracking and delayed cracking in hardenable steels, believed to be caused by hydrogen absorbed during welding, can be promoted in parallel with the severity of micro and macrosegregation. Again, the solute rich regions which are the last to experience austenite-martensite transformation become enriched in hydrogen as it has lower solubility in martensite than in austenite.

In steady current arc welding, weld pool shape under steady-state heat flow depends on heat input, arc travel speed, and thermal properties of the material. The first two of the three variables may have some flexibility to allow a more favorable pool shape to form. However, this flexibility is gained at the expense of welding efficiency. In pulsed current arc welding, on the otherhand, ability to dissipate heat between pulses should allow a wider range of parameters for control of weld pool shape.

As an inquiry into the extent of the additional control gained by pulsing, for thin sheet welding, dimensions of the autogenous PC-GTA welds on 0.032 in. (0.081 cm) thick sheets of the Fe-26Ni alloy were measured. Weld pool shapes using the dimensions defined in Figure 3, are tabulated in Table 5. Tangent ϕ, defined as D/2L, is intended as a rough measure of the grain growth direction which, for elliptical pools, changes continually from weld fusion line to the centerline.

The effects of the weld process parameters on weld nugget area, weld bead width back to front ratio (d_b/d_f) were presented in the first annual report[2]. As expected, increasing high pulse current (i_p), and consequently heat input (H), for constant i_b, t_p, t_b and arc travel speed (v) resulted in larger d_b/d_f ratios, larger nugget areas and higher melting efficiencies. More significantly some increases in d_b/d_f, nugget area and melting efficiency were obtained with decreasing pulse frequency alone, while all other variables, including the heat input, were kept constant. Increase in d_b/d_f ratio, which was 14% when the pulse frequency was reduced from 48 to 1, indicated increased penetration control capability with pulsing under constant heat input conditions.

In addition to the above mentioned effects of pulsing on weld bead dimensions, weld pool shape was also found to be dependent on the pulsing parameters selected. For example, d_b/d_f ratios of 0.95 and higher could be obtained while tan ϕ ranged from 0.51 to 0.74 for an arc travel speed of 0.212 $cm.s^{-1}$. When the arc travel speed was increased to 0.605 $cm.s^{-1}$, tan ϕ could drop considerably to around 0.30 (Table 5).

Pulse frequency was the most influential of the pulsing parameters in determining weld pool shape, as characterized by weld pool elongation (L) and maximum pool (or bead) width (D) and their ratios (tan ϕ). This is seen in Figure 4. For constant H, i_p, i_b, and v, pulse frequency could be changed by changing t_p and t_b while keeping their ratio constant. The effects of pulse frequency and t_p were, therefore, coincidental and could not be separated.

For pulse frequencies below 3 Hz where the frequency effect on tan ϕ seems to be small (Figure 4), the pool shape was found to be indicative of the melting efficiency of the process up to a melting efficiency of about 28% as shown in Figure 5. The minimum on the tan ϕ curve in this figure is probably due to the higher rate of increase in D for high melting efficiencies when d_b/d_f ratio no longer increases. On the otherhand, weld pool elongation (L) and melting efficiency are directly proportional.

Arc travel speed has strong influence on tan ϕ and pool trailing edge radius (r) as indicated in Figures 6 and 7. With higher speeds of arc travel weld pool elongates considerably and trailing edge radius is reduced, conditions which may affect weld mechanical properties first due to the increased centerline segregation, and second because of the notch effect that is possible with small trailing edge radii.

These results indicate that for materials sensitive to centerline cracking pulse frequency and arc travel speed should be kept low.

3.1.2 Grain Size and Solidification Structure

During weld pool solidification heat affected zone grains in the parent metal act as substrate for the growth of weld metal grains. This occurs without a nucleation event and the growing weld metal grains follow the same crystallographic orientation[6]. The resultant grains are usually columnar in shape and, as mentioned above, tend to follow the weld pool isotherms. In doing this, they may go through a process of competitive growth which, in most steady current welding situations, is the only grain size determining process.

Columnar to equiaxed growth transitions in welds are relatively rare because the conditions favoring the development of equiaxed grains ahead of the columnar crystals are not frequently established. Grain multiplication mechanism, an important source of new crystals[7], cannot operate apparently because the dendrite fragments separated from growing dendrites cannot survive in the severe thermal climate of the weld pool. High alloy contents and high welding speeds should, however, promote equiaxed weld metal solidification in the weld center where the thermal gradients (G_L) can be very small and the solidification rates (R) can be very high. Examples of this possibility have been reviewed by Davies and Garland[8]. The welding speeds of 1 m/min. or higher have been used to develop an equiaxed region, in comparison the highest welding speed employed in the present study was 0.36 m/min.

Pulsed current arc welding, on the otherhand, should be more flexible in obtaining the right conditions for equiaxed crystal growth, both in terms of obtaining a low G/R ratio and bringing to the solidification front heat pulses necessary for crystal fragmentation, as well as transport. In full penetration welding of thin sheets, however, added flexibility by pulsing is reduced by the necessity to keep d_b/d_f ratio high, to prevent burn through and to maintain weld seam continuity.

A full penetration weld here has been arbitrarily defined as a weld whose bead widths at the back and the front are within 5% of each other, or

$$\frac{d_b}{d_f} \geq 0.95$$

This definition eliminates some of the thin sheet welds listed in Table 2, series F through M, from being considered as welds made under two dimensional heat flow conditions. Welds with lower heat inputs are thus eliminated. Similarly, welds with high inputs tended to produce burn throughs (welds F2, G6, J9) so that the range of arc energies used to produce full penetration welds in the 0.032 in.

(0.08 cm) thick Fe-26Ni alloy was roughly 400-600 cal. cm^{-1}. In addition, higher arc pressures developed under high i_p values (such as welds G6, J9, J10 and J11) also caused burn throughs. Equipment limitation relative to attaining lower arc travel speeds than used (e.g., 0.212 $cm.s^{-1}$) was another constriction on the parametric flexibility of the pulsed arc process. Consequently, possible grain refining effect of pulsing was severely limited, and, in fact, for none of the full penetration welds columnar to equiaxed transition was observed.

All weld surfaces exhibited a superficial grain structure that were separate from the solidification structure. This superficial surface structure typically seen in Figure 8, although complicating the metallographic analysis, could easily be polished away to reveal the solidification structures as in Figure 9. The "surface" and the real grains were quite similar in size, so that the effect of pulsing parameters on grain size could be approximately determined from observing as welded surfaces of the specimens.

Tentative indications are that for full penetration welds ($d_b/d_f \geq 0.95$) when tan ϕ (Table 5) is less than 0.4, welds did not develop a continuous centerline grain. Some high pitch-high heat input welds (F5, F6, G5 and G8) were also without a continuous centerline grain even though tan ϕ values were above 0.5, while others contained a continuous center grain. A full penetration weld with a tan ϕ value of 0.4 or less largely consisted of grains whose length was 1/2 of bead width (1/2 d_f) or slightly larger. Here the grains growing from either side of the weld met at the centerline, and there was some competition among them, precluding any grain refinement.

All full penetration welds with tan ϕ values higher than 0.5 developed grains that frequently extended much longer than 1/2 d_f following the elliptical solidification isotherm. Here again competetive growth process frequently resulted in increased grain width near the weld center. Only those welds made with low heat input ($H < 400$ $cal.cm^{-1}$)

resulting in d_b/d_f values much less than 0.95 showed development of new grains all around the solidification isotherm. This group includes welds F1, F4, F8, G1, G2, J2, K5, L3 and L5.

The significant observation here is that for the full penetration welds, only those with the highest heat inputs and relatively large pitches did not develop a continuous center grain. Perhaps, indicating that if the above discussed restrictions were absent, conditions could be created for more prevalent grain multiplication. Such conditions, i.e., lower G_L, higher R values, could mean the use of higher heat inputs and pitch values.

Solidification substructure was mainly cellular (Figure 9), but in some welds dendritic growth was also observed. The latter mainly in low heat input welds or just prior to the initiation of high pulse current arc. Cellular continuity was largely unaffected by the weld pool waves created by arc pressure changes or turbulant flow created by Lorentz's force.

3.1.3 Weld Surface Ripple Formation

Most weld surfaces normally show ripple formations. The pulsed current GTA welds made on thin sheets of the Fe-26Ni alloy in the present investigation exhibited ripples that were periodic, reproducible and symmetrical about the weld centerline. The distance between the easily recognizable primary ripples was in all cases equal to the pitch (P) of the process (see Figure 8), and less intense secondary ripples between them had spacings that were remarkably repetitive from one pitch to the next.

Such reproducible and periodic nature of the ripples was considered as a possible "fingerprint" relating weld pool kinetics and the movement of the solidification front. Consequently, an inquiry was made into the ripple characteristics and the mechanism of their formation largely through observations by ordinary light and electron optics and by high speed cinematography.

Weld surface ripples have, in the past, caught the attention of several investigators[9-13] and a number of theories have been suggested to explain their formation. For example, D'Anessa[9] proposed that interaction of growth rate fluctuations and surface tension effects was responsible for the ripples. Garland[10], on the otherhand, concluded that the ripples could not be due to growth rate fluctuations, but were related to the cyclic current supply. He, then, suggested a mechanism involving an interface/liquid surface interaction at rapid rates of solidification. Earlier works by Cheever and Howden[11] and by Movchan[12] attributed ripples to the existence of growth rate fluctuations caused by the solid-liquid interface instability presumed to be inherent to rapid solidification. Later, Kotecki, Cheever and Howden[13] showed that pool oscillations caused by the physical pressure of an arc plasma produced the ripples. It is with this final proposal that our observations seem to agree.

After reviewing the high-speed motion pictures of eleven welds made on thin sheets of the Fe-26Ni alloy, the following main features of the mechanism of formation of weld surface ripples in pulsed current welding have emerged.

Onset of high current arc exerts a sudden pressure on the weld pool. This causes the weld pool to stretch and the molten metal pushed aside creates a circular wave which resembles that caused by a stone thrown into a lake. Except that in this case a mirror image of the wave also forms at the back surface of the pool. The wave advances toward the sides of the pool, and when it meets the growing solid at the pool edges, it provides a small amount of molten metal above the plane of the solid weld surface (at the back of the weld the wave provides molten metal below the plane of the solid weld surface) enough to produce some solid growth normal to the weld plate. Such growth occurs all along the solidification isotherm constituting a ripple on the solidified weld metal. Successive waves interact with the solid-liquid interface slowly losing their amplitude and thus causing the formation of ripples of successively lower visibility.

Upon $i_p \rightarrow i_b$ transition removal of the arc pressure creates another series of waves that result in similar ripples. Figure 10 depicts the initiation and movement of the first wave that forms after the high current arc is turned off. Wave formations and their travel could be followed by observing the reflection of the hot electrode tip in the weld pool.

Transitions from a high current arc to a low current arc in the present welds were extremely rapid, completing within about one milisecond. Consequently, sudden onset of arc pressure which has been shown to be proportional to the square of the Direct Current gas tungsten arc current[14] could have an impact sufficient to cause the formation of a wave. The force of a 150A arc for an initial arc gap of 2.5 mm, roughly estimated from Erokhin's[14] results, is about 1.25 gram force (1.2×10^{-2}N) capable of accelerating 1.25 gram mass at one meter per second square. An average weld pool, on the other hand, consisted of only about 0.6 g of molten metal. Of course the arc force would also be opposed by the surface tension of the pool on both sides of the weld (top and bottom), thus holding the weld pool together.

High magnification examination of the ripples shows that they consist of a series of individual spikes protruding up from the weld metal surface (Figure 11). The spikes tend to be located at the underlying cell boundaries (Figure 12) indicating, perhaps, that elsewhere spike formation is restricted by nucleation difficulty.

If the ripples form when waves periodically provide molten metal above or below the planes of the weld top or bottom surfaces, as suggested above, they should then reflect the chemistry of the solute rich boundary layer just ahead of the solid-liquid interface. This was clearly the case when spikes and spike free areas of the weld metal surface on sample G5 were analyzed by the energy dispersive x-ray method. Approximately calculated percentages of silicon and manganese, minor elements in the bulk alloy, were considerably higher in the spikes than found in the nearby flat areas. Table 6 gives the compositional ratios of five elements found in the spikes. Aluminum

was not intentionally added to the melt, consequently, its presence in spikes No. 6, 7 and 8 was unexpected and requires clarification. These spikes, especially Nos. 6 and 7, may have contained oxides of Al and Si and perhaps aluminum contamination is either from the melt mix or the crucible. The different chemical partitioning between different locations on the weld may also reflect the mixing effect of increased fluid flow during high pulse time. Further possibilities include the influence of the changing rate of advance of the solidification front, and the changing amplitude of the oncoming waves. Obviously, a more complete picture of the chemical partitioning between the ripple spikes and the bulk weld surface requires more definitive experimental inquiry.

3.1.4 Solidification Rates From Ripples

Aside from acting like markers showing the shape of solidification isotherms along the weld seam,weld surface ripples may contain other information that could be useful in analysis of weld pool phenomena and, perhaps, in weld quality assurance. One such information is their spacing. Under some controlled welding conditions, such as those that could exist in mechanized welding, the repetitive nature of the ripples could provide clues to any momentary fluctuation in the weld solidification rate or to the formation of weld defects.

In analysis of weld solidification under pulsed welding conditions, one of the determinants is the solidification rate. Although the average rate is equal to the arc travel speed, the pulsed nature of the heat input dictates periodic increases and decreases in the rate of solidification. Measurements of such variation, which is consequential to the present work, may be possible from the ripple spacings.

Experimentally determined times for successive weld pool waves reaching the trailing edge of the pool are tabulated in Table 7. It is seen that after the second or third wave, a relatively constant wave period is reached, yet the secondary ripple spacings, as seen in Figure 11, change with distance along the weld axis. The unequal

ripple spacings result from the variations in the solidification rate between pulses. It should, therefore, be possible to determine incremental rates of solidification from ripple spacings.

In Figure 13 a comparison is made between the measurements of solid-liquid interface displacement after $i_p \rightarrow i_b$ transition for weld J7. Only the displacement of the trailing edge of the weld pool is measured. Measurements obtained from ripple spacings of two different welds of J7 parameters are remarkably close. Agreement with the displacement measurements from a motion picture is also good.

The tendency for the weld pool wave periods to reach a constant value after the second or the third wave will allow estimates of solid growth rates to be determined from secondary ripple spacings. An additional information that can be obtained from ripples is the average growth and growth rates for high pulse and low pulse periods. The transitions from i_p to i_b and vice versa create waves that have high amplitudes initially. The first ripples that form after each transition, therefore, are markedly more visible than the others. Measurements of the distance between these high intensity ripples then gives the total solid-liquid interface displacements during t_p or t_b or $t_p + t_b$. Table 8 is a list of such measurements showing growth during t_p and t_b, as well as the corresponding average growth rates. When there is no growth, (Sp = 0), there is the possibility of a melt back after $i_b \rightarrow i_p$ transition. Indications are that when there is an appreciable melt back the major ripples thus formed show a flattening of the trailing edge of the ripple (pool trailing edge radius, r, increases while others remain the same). This effect is quite noticeable on welds made on thicker plates.

Table 8 shows that the growth rates in t_p and t_b periods of a cycle can differ considerably and as shown in Figure 14 may be manipulated by the selection of pulsing parameters, in this case pulsing frequency.

3.2 Welds on Plates

Analyses of the effects of pulsing parameters on weld bead and pool size and shape, as well as the solidification structures for the welds made on Fe-26Ni and Fe-36Ni alloy plates are presently underway. These welds, listed in Table 2 as weld series N through S and in Table 3 as series T, show a more varied grain structure and substructure than were observed in thin sheet welds, mainly because of the much faster cooling rates associated with them. The more massive chilling provided by the thicker weld plate, for example, resulted in the elimination of the continuous weld centerline grain and in fact resulted in an equaxed grain structure in sample P6 as against the sample N6 as seen in Figure 15.

Further welds in the 30 mm thick plates of Fe-36Ni are planned using a different power supply capable of providing peak currents in excess of 150 amperes which is the maximum current capability of the unit used up to now.

3.3 Pulsing Effects on Segregation

A study of the effect of pulsing parameters on solute segregation in the weld fusion zone has been initiated to determine if the periodically varying cooling rates created due to pulsing reduces the solute transport and buildup along the weld seam or, in fact, results in periodic high solute concentrations (banding).

The extent and method of transport of alloy elements and impurities transverse and parallel to the welding direction is a fundamental question which bears upon several practical concerns in welding. The buildup of elements and impurities has been shown to be linked with one type of weld cracking. Repeated banding parallel to the growth interface (perpendicular to the travel direction) may be influenced by solute transport and deposition.

This brief study is aimed at determining the extent of this transport. Sulfur will be the indicator of solute transport. A set of experiments has been started using a high sulfur steel in the weld plate and autogenous bead-on-plate type welds made with or without arc current pulsing. Table 4 lists the welding parameters used for the two pulsed and two steady current welds made initially. A sulfur print of the four welds is shown in Figure 16. Although the welds V2 and V4 were similar in size, some centerline segregation of sulfur (toward the top of the weld seam in the figure) in weld No. V4 is indicated while no such segregation is visible in V2, the pulsed current weld.

4.0 COMPUTATION PROCEDURES FOR PULSED ARC WELDING

The thermal behavior of sheets and plates welded by the pulsed arc process is being simulated by computer models. A version to simulate pulsed welding of sheets considers conduction in two dimensions (parallel and perpendicular to the welding direction in the plane of the sheet). The two dimensional version can account for convective heat transfer from the top and bottom surfaces. The version to simulate welding of plates is under initial development and will be based on three dimensional transient conduction. Again, convective losses will be taken into account. Due to the cyclic nature of pulsed welding, transient heat conduction analysis is used in which the arc (heat source) is considered to move in small increments relative to the workpiece. The thermal fields close to the weld zone as well as positions distant from the weld zone are described by the simulations and attempts are being made to use finer node spacings to give better resolution. Presently, the analysis does not account for volume changes. It is essentially for autogenous welds; and it will not simulate the deposition of multiple beads.

The basic equation for transient conduction analyses

$$\rho C_p \frac{\partial T}{\partial \theta} = \nabla (k \nabla T) \qquad (1)$$

is converted from differential form to finite differences for the computer simulation. For two dimensions, equation 1 would be rewritten with reference to a two dimensional array of nodes in finite difference form

$$T'_{m,n} = \frac{k}{\rho C_p} \frac{\Delta\theta}{\Delta x^2} (T_{m,n+1} + T_{m,n-1} - 2T_{m,n}) + \frac{\Delta\theta}{\Delta y^2} (T_{m+1,n} + T_{m-1,n} - 2T_{m,n}) + T_{m,n} \qquad (2)$$

where $T'_{m,n}$ $T_{m,n}$ = temperature at node m,n after and before a time interval $\Delta\theta$ in duration.

Less generally for a square array

$$T'_{m,n} = \frac{1}{S} [T_{m,n+1} + T_{m,n-1} + T_{m+1,n} + T_{m-1,n} + (S-4)\ T_{m,n}] \quad (3)$$

where $S = \frac{\Delta x^2}{\alpha \Delta\theta}$

$\Delta x = \Delta y$

$\alpha = k/\rho C_p$

Stable solutions to equation 3 may be found for values of S greater than 4, although better accuracy (and more computation time) is obtained for larger values of S. A heat source or sink for the element represented by node m,n would be taken into account by modifying equation 3:

$$T'_{m,n} = \frac{1}{S} [T_{m,n+1} + T_{m,n-1} + T_{m+1,n} + T_{m-1,n} + (S-4)T_{m,n} + \frac{Q}{\delta k}] \quad (4)$$

Convection from surfaces can be taken into account in a similar fashion.

The process of using the finite difference technique to find a solution for the thermal conditions in pulsed arc welding requires several steps: some steps are built into the computer program for repeated use; some are automatically determined by the program based on the conditions of interest; and some are input by the user based on the conditions to be simulated.

4.1 The Network for Sheet Welding

In the first year the sheet was considered to be divided into square elements with a node at the center of each element. Node spacings of 0.1 to 0.2 cm were used.

A refinement was made in the current year to give more resolution near the arc. The sheet was divided into square elements

of two sizes; five columns away from the arc were 0.1 cm on a side and ten columns near the arc were 0.05 cm on a side. About 85 rows of the small square element were utilized.

Presently, greater refinement is being sought together with a decrease in the time of computation by using a large square grid of spacing Δx_L with a smaller grid of spacing Δx_S around the arc. The extent of the small grid M_S, N_S and the ratio of Δx_L to Δx_S are set by the user depending on the conditions and the degree of resolution desired. A central region within the small grid which includes the liquid pool is treated differently than the rest of the small grid as described later.

The problem is initialized by setting the temperature of each node to the plate temperature. If there is no preheat, room temperature is used for all nodes in the two dimensional M by N array (or for the two M by N and M_S by N_S arrays in the newest technique).

4.2 Arc Coverage and Movement

In the first versions of the program the arc was considered to cover a single element (node) and the arc was moved to another node in stops of Δx whenever the number of iterations since the last incremental move, N_a, satisfied the condition

$$N_a \, \Delta\theta = \frac{\Delta x}{v} \tag{5}$$

where v = arc travel speed, cm/sec.

At the time the arc is moved, the grid points are renumbered to add one more row of elements to the leading edge of the sheet and to remove one row of elements from the trailing end of the sheet. The heat input to the node covered by the arc is q/2 due to symmetry.

In the latest version of the program the arc (heat source) is considered to cover several elements and to move after each interval of time, $\Delta\theta$. Considering one of the nodes in the arc region to be numbered $m_{arc,1}$ the initial arc coverage is given in the table below.

Nodes	Initial Heat Input	Half Step Heat Input
$m_{arc},1$	q/14	q/14
$m_{arc}-1,1$	q/14	q/14
$m_{arc}-2,1$	0	q/28
$m_{arc}+1,1$	q/14	q/28
m_{arc} 2	q/7	q/8
$m_{arc}-1,2$	q/14	q/8
$m_{arc}-2,2$	0	q/56
$m_{arc}+1,2$	q/14	q/56

After each time interval $\Delta\theta$, the arc coverage is considered to move forward an amount

$$x_a = v\Delta\theta \tag{6}$$

and thus move a fraction of an element $x_a/\Delta x_s$. When this fraction equals one half, the arc coverage would be as given in the table above. After the number of iterations given by relation (5) the elements are renumbered.

4.3 Conductivity/Convection in the Liquid Zone

Fluid motion in the liquid pool due to steep thermal gradients, arc pressure, and magnetic fields would account for greater transfer of heat and more uniform temperatures in the liquid pool than by conduction alone. In the absence of a detailed model of fluid motion, the expedient of using an exaggerated thermal conductivity for the liquid has been applied. Thus, the thermal conductivity of the solid is multiplied by a factor (which may be set by the user) to calculate conduction in nodes above the solidus temperature. In previous simulations of casting processes, factors of 5 to 7 have been adequate.

4.4 Computation

After the temperature at each nodal point has been initialized the value(s) of $\Delta\theta$ must be selected such that the parameter S in equation 3 is greater than 4. In the initial programs with a uniform node spacing, this meant that

$$\Delta\theta \leq \frac{\Delta x^2 \rho C_p}{4 F k} \tag{7}$$

where F is the factor multiplying the thermal conductivity of solid to get the exaggerated thermal conductivity of the liquid. A value of S equal to 4 would give stability with minimum accuracy in the liquid pool and greater accuracy in the solid regions.

Assuming no convection from the surfaces of the plates, equation 3 would be used to compute new temperatures at every node without arc coverage and equation 4 would be used to calculate new temperatures at the node(s) with arc coverage. For the first calculation the initial temperatures are the prior temperatures, i.e., unprimed temperatures in equations 3 and 4. For subsequent computations all new temperatures are calculated based on the temperatures calculated for the end of the previous time step.

For the latest version three time steps may be used. The program searches the temperature array in the small grid around the arc to determine which elements are above the solidus temperature. For these elements where convection and conduction occur

$$\Delta\theta_C = \frac{\Delta x_s^2 \rho C_p}{4 F k} \tag{8}$$

For the rest of the small grid and the large grid

$$\Delta\theta_S = F\Delta\theta_C \tag{9}$$

$$\Delta\theta_L = \left(\frac{\Delta x_L}{\Delta x_S}\right)^2 \Delta\theta_S \tag{10}$$

For every iteration to compute new temperatures in the coarse grid, there must be $(\Delta x_L/\Delta x_S)^2$ iterations within the solid regions of the fine grid and $F(\Delta x_L/\Delta x_S)^2$ iterations within the liquid regions of the fine grid.

4.5 Output

The results of calculations can be output from the computer in many forms. Usually the calculations are performed for sufficient pulsing cycles to consider the arc to be at psuedo steady state, the temperature distribution at equivalent states of the pulse cycle is the same from pulse to pulse. Then the array of temperatures for the stage(s) of the pulse of interest are printed after every interval $\Delta\theta$ or after every n_p intervals, where n_p is set by the user.

4.6 Three Dimensional Model

The grid for the three dimensional simulation of pulsed welding in plates is similar to the grid in the latest version of the sheet program. The elements are cubes with a node in the center of each cube. The volume around the arc is subdivided into smaller cubes by an integral factor set by the user. Again the calculation uses different time steps for the liquid zone, the rest of the region of small node spacing, and the volume with large node spacing. The nodes and corresponding temperatures are now three dimensional arrays, M by N by P, and the three dimensional version of equation 4 would be:

$$T'_{m,n,p} = \frac{1}{S}\left[T_{m,n+1,p} + T_{m,n-1,p} + T_{m+1,n,p} + T_{m-1,n,p} + T_{m,n,p+1} + T_{m,n,p-1} + (S-6)\,T_{m,n,p} + \frac{Q}{\delta k}\right] \tag{11}$$

Again, the arc coverage is spread over eight nodes and is considered to move a small increment after each time step.

REFERENCES

1. M. G. Vassilaros, et.al., "Heat Flow Model of Pulsed Arc Welding", to be published.

2. G. M. Ecer, et.al., "Investigation of Weld Pool Structure and Property Control in Pulsed Arc Welding", Annual Progress Report to ONR, Oct. 31, 1978.

3. A. Tzavaras, et.al., "Effect of Welding Parameters on Solidification Structures in Pulsed GTA Welded Fe-26Ni", TMS-AIME, Fall Meeting, St. Louis, MO (Oct. 1979).

4. C. M. Adams, Jr., "Cooling Rates and Peak Temperatures in Fusion Welding", Welding J., 37 (5) Res. Suppl. 210s to 215s (1958).

5. A. A. Wells, "Heat Flow in Welding", Welding J., 31 (5) Res. Suppl. 263s to 267s (1952).

6. W. F. Savage and A. H. Aronson, "Preferred Orientation in the Weld Fusion Zone", Welding J., 45 (2) Res. Suppl. 85s to 89s (1966).

7. M. C. Flemings, Solidification Processing, McGraw Hill Book Co., New York, p. 154 (1974).

8. G. J. Davies and J. G. Garland, "Solidification Structures and Properties of Fusion Welds", Int. Met. Reviews, 20, pp. 83-106 (1975).

9. A. T. D'Annessa, "Sources and Effects of Growth Rate Fluctuations During Weld Metal Solidification", Welding J., 49 (2) Res. Suppl. 41s to 45s (1970).

10. J. G. Garland, G. J. Davies, "Surface Rippling and Growth Perturbations During Weld Pool Solidification", Met. Constr. and British Welding J., 2 (5) 171-175 (1970).

11. D. L. Cheever and D. G. Howden, "Nature of Surface Ripples", Welding J., 48 (4) Res. Suppl. 179s to 180s (1969).

12. B. A. Movchan and Sh. A. Abitdinor, "Movement of the Inter-Phase Boundary When Spot Welds Solidify", Automatic Welding, 21 (12) 4-8 (1968).

13. D. J. Kotecki, D. L. Cheever, and D. G. Howden, "Mechanism of Ripple Formation During Weld Solidification", Welding J. 51 (8), Res. Suppl. 386s to 391s (1972).

14. A. A. Erokhin, et.al., "The Force Effect of the Pulsed Arc on Weld Metal", Automatic Welding, 29 (5) 4-6 (1976).

TABLE 1

DEFINITIONS OF SYMBOLS USED

Parameter	Symbol	Definition	Units
High Pulse Current	i_p	See Figure 1	A
Low Pulse Current	i_b	See Figure 1	A
High Pulse Time	t_p	See Figure 1	s
Low Pulse Time	t_b	See Figure 1	s
Pulse Frequency	f	$1/(t_p + t_b)$	Hz
Temperature	T	--	°C or °K
Arc Travel Speed	v	--	$cm.s^{-1}$
Pitch	P	$v(t_p + t_b)$	cm
Sheet Thickness	δ	--	cm
Weld Bead Width	d or d_b or d_f	See Figure 3	mm
Weld Pool Elongation	L	See Figure 3	mm
Pool Trailing Edge Radius	r	See Figure 3	mm
Grain Angle	ϕ	See Figure 3	Degrees
Arc Current	i	--	A
Arc Voltage	e	--	V
Total Arc Energy per Unit Length	H	$\frac{i \cdot e}{v}$	$0.239\ cal.cm^{-1}$
Net Energy Input per Unit Length	H_{net}	$\mu_1 \cdot H$	$cal.cm^{-1}$
Heat Transfer Efficiency	μ_1	H_{net}/H	%
Melting Efficiency	μ_2	H_m/H	%
Rate of Heat Input per Unit Sheet Thickness	q	$\frac{v.H_{net}}{\delta}$	$cal.s^{-1}.cm^{-1}$
Rate of Heat Input	Q	$q \cdot \delta$	$cal.s^{-1}$
Thermal Conductivity	k	--	$cal.s^{-1}.cm^{-1}.K^{-1}$
Density	ρ	--	$g.cm^{-3}$
Specific Heat	C_p	--	$cal.g^{-1}.K^{-1}$
Thermal Diffusivity	α	$\frac{k}{C_p \cdot \rho}$	$cm^2.s^{-1}$
Time	θ	--	s

TABLE 2

AUTOGENOUS GTA WELDS ON THE Fe-26Ni ALLOY

Weld No.	δ (cm)	i_p (A)	i_b (A)	t_p (s)	t_b (s)	v ($cm.s^{-1}$)	t_p/t_b	f (Hz)
F1	0.08	100	10	0.017	0.167	0.212	0.10	5.4-I.P.*
F2	0.08	100	10	0.100	0.167	0.212	0.60	3.7-B.T.*
F3	0.08	100	10	0.067	0.167	0.212	0.40	4.3
F4	0.08	100	10	0.033	0.167	0.212	0.20	5.0
F5	0.08	100	10	0.167	0.333	0.212	0.50	2.0
F6	0.08	100	10	0.133	0.333	0.212	0.40	2.1
F7	0.08	100	10	0.067	0.333	0.212	0.20	2.5
F8	0.08	100	10	0.050	0.333	0.212	0.15	2.6
G1	0.08	80	10	0.167	0.667	0.212	0.25	1.2
G2	0.08	100	10	0.167	0.667	0.212	0.25	1.2
G3	0.08	120	10	0.167	0.667	0.212	0.25	1.2
G4	0.08	120	10	0.167	0.667	0.212	0.25	1.2
G5	0.08	140	10	0.167	0.667	0.212	0.25	1.2
G6	0.08	150	10	0.167	0.667	0.212	0.25	1.2-B.T.*
G7	0.08	110	10	0.167	0.667	0.212	0.25	1.2
G8	0.08	130	10	0.167	0.667	0.212	0.25	1.2
H1	0.08	100	20	0.167	0.667	0.212	0.25	1.2
H2	0.08	100	25	0.167	0.667	0.212	0.25	1.2
H3	0.08	100	5	0.167	0.667	0.212	0.25	1.2
H4	0.08		I=24A	Steady Current		0.212	--	--
H5	0.08		I=28A	Steady Current		0.212	--	--
H6	0.08		I=32A	Steady Current		0.212	--	--
H7	0.08		I=36A	Steady Current		0.212	--	--
H8	0.08		I=40A	Steady Current		0.212	--	--
J1	0.08	120	10	0.004	0.017	0.212	0.25	47.8
J2	0.08	120	10	0.008	0.033	0.212	0.25	24.3
J3	0.08	120	10	0.017	0.067	0.212	0.25	12.0-B.T.*
J4	0.08	120	10	0.033	0.133	0.212	0.25	6.0
J5	0.08	120	10	0.067	0.267	0.212	0.25	3.0
J6	0.08	120	10	0.133	0.533	0.212	0.25	1.5
J7	0.08	120	10	0.208	0.832	0.212	0.25	1.0
J8	0.08	150	10	0.083	0.565	0.212	0.15	1.5
J9	0.08	150	10	0.042	0.167	0.212	0.25	4.8-B.T.*
J10	0.08	150	10	0.033	0.250	0.212	0.13	3.5-B.T.*
J11	0.08	150	10	0.025	0.250	0.212	0.10	3.6-B.T.*
K1	0.08	120	10	0.042	0.286	0.212	0.15	3.0
K2	0.08	120	10	0.042	0.212	0.212	0.20	3.9
K3	0.08	120	10	0.042	0.167	0.212	0.25	4.8
K4	0.08	120	10	0.042	0.135	0.212	0.31	5.6-B.T.*
K5	0.08	120	10	0.083	0.572	0.212	0.15	1.5
K6	0.08	120	10	0.083	0.426	0.212	0.20	2.0
K7	0.08	120	10	0.083	0.333	0.212	0.25	2.4
K8	0.08	120	10	0.125	0.500	0.212	0.25	1.6
K9	0.08	120	10	0.167	0.667	0.423	0.25	1.2
K10	0.08	120	10	0.167	0.333	0.423	0.50	2.0

TABLE 2 (cont.)

Weld No.	δ (cm)	i_p (A)	i_b (A)	t_p (s)	t_b (s)	v (cm.s^{-1})	t_p/t_b	f (Hz)
L1	0.08	120	10	0.167	0.250	0.423	0.67	2.4
L2	0.08	120	10	0.083	0.125	0.423	0.66	4.8-B.T.*
L3	0.08	120	10	0.083	0.333	0.423	0.25	2.4
L4	0.08	120	10	0.083	0.167	0.423	0.50	4.0
L5	0.08	120	10	0.083	0.167	0.605	0.50	4.0
L6	0.08	120	10	0.167	0.333	0.605	0.50	2.0
L7	0.08	120	10	0.167	0.250	0.605	0.67	2.4
L8	0.08	150	10	0.167	0.333	0.605	0.50	2.0
M1	0.08	150	10	0.038	0.250	0.212	0.15	3.5
M2	0.08	150	10	0.050	0.250	0.212	0.20	3.3
M3	0.08	150	10	0.208	0.333	0.576	0.62	1.8
M4	0.08	150	10	0.021	0.033	0.576	0.62	18.5
N1	0.14	150	10	0.025	0.250	0.212	0.1	3.6
N2	0.14	150	10	0.050	0.250	0.212	0.2	3.3
N3	0.14	150	10	0.100	0.250	0.212	0.4	2.9
N4	0.14	150	10	0.250	0.250	0.212	1.0	2.0
N5	0.14	150	10	0.250	0.500	0.212	0.5	1.3
N6	0.14	150	10	0.250	0.832	0.212	0.3	0.9
P1	0.25	150	10	0.025	0.250	0.212	0.1	3.6
P2	0.25	150	10	0.050	0.250	0.212	0.2	3.3
P3	0.25	150	10	0.100	0.250	0.212	0.4	2.9
P4	0.25	150	10	0.250	0.250	0.212	1.0	2.0
P5	0.25	150	10	0.250	0.500	0.212	0.5	1.3
P6	0.25	150	10	0.250	0.832	0.212	0.3	0.9
Q1	0.30	150	10	0.025	0.250	0.212	0.1	3.6
Q2	0.30	150	10	0.050	0.250	0.212	0.2	3.3
Q3	0.30	150	10	0.100	0.250	0.212	0.4	2.9
Q4	0.30	150	10	0.250	0.250	0.212	1.0	2.0
Q5	0.30	150	10	0.250	0.500	0.212	0.5	1.3
Q6	0.30	150	10	0.250	0.832	0.212	0.3	0.9
R1	0.30	150	10	0.050	0.100	0.212	0.5	6.7
R2	0.30	150	10	0.025	0.050	0.212	0.5	13.3
R3	0.30	150	10	0.015	0.030	0.212	0.5	22.2
R4	0.30	150	10	0.005	0.010	0.212	0.5	66.7
R5	0.30	150	10	0.050	0.050	0.212	1.0	10.0
R6	0.30	150	10	0.010	0.010	0.212	1.0	50.0
S1	0.30	150	10	0.015	0.075	0.212	0.2	11.1
S2	0.30	150	30	0.015	0.075	0.212	0.2	11.1
S3	0.30	150	50	0.015	0.075	0.212	0.2	11.1
S4	0.30	I = 40 Amps - Steady Current						N.M.*
S5	0.30	I = 50 Amps - Steady Current						N.M.*
S6	0.30	I = 60 Amps - Steady Current						
S7	0.30	I = 70 Amps - Steady Current						
S8	0.30	I = 80 Amps - Steady Current						

*Comments: I.P. - Incomplete Penetration; B.T. - Burn-Through; N.M. - No Melting

TABLE 3

AUTOGENOUS BEAD-ON-PLATE GTA WELDS MADE ON A 30 mm THICK PLATE OF THE Fe-36Ni ALLOY

Weld No.	δ (cm)	i_p (A)	i_b (A)	t_p (s)	t_b (s)	v ($cm.s^{-1}$)	t_p/t_b	f (Hz)
T1	3.0	150	10	0.050	0.050	0.212	1.0	10
T2	3.0	150	10	0.010	0.010	0.212	1.0	50
T3	3.0	150	10	0.005	0.005	0.212	1.0	100
T4	3.0	150	10	0.250	0.250	0.212	1.0	2
T5	3.0	150	10	0.250	0.250	0.212	1.0	2
T6	3.0	I = 100A		Steady Current		0.212	--	--
T7	3.0	I = 120A		Steady Current		0.212	--	--
T8	3.0	I = 80A		Steady Current		0.212	--	--

TABLE 4

AUTOGENOUS BEAD-ON-PLATE GTA WELDS
MADE ON A HIGH SULFUR STEEL PLATE*

Weld No.	δ (cm)	i_p (A)	i_b (A)	t_p (s)	t_b (s)	v ($cm.s^{-1}$)	t_p/t_b	f (Hz)
V1	0.30	130	10	0.167	0.667	0.212	0.25	1.2
V2	0.30	150	10	0.250	0.250	0.212	1.00	2.0
V3	0.30	I = 80A, Steady Current			--	0.212	--	--
V4	0.30	I = 110A, Steady Current			--	0.212	--	--

*Nominal Composition: Fe - 0.13 Max C - 0.85 Mn - 0.10 P - 0.30 S.

TABLE 5

WELD POOL DIMENSIONS

Weld No.	D (mm)	d (mm)	d_b/d_f	D-d (mm)	L (mm)	r (mm)	tan ϕ
F1	2.7	2.7	0	--	1.3	1.3	1.04
F3	6.7	6.7	0.97	--	5.4	1.2	0.62
F4	3.8	3.8	0.79	--	2.7	1.1	0.70
F5	8.9	8.7	0.99	0.2	6.6	1.5	0.67
F6	7.4	7.4	0.95	--	7.2	1.6	0.51
F7	4.7	4.7	0.85	--	3.7	1.0	0.63
F8	3.5	3.5	0.57	--	2.3	1.4	0.76
G1	4.1	3.8	0.73	0.3	2.8	1.4	0.73
G2	5.5	5.2	0.83	0.3	4.7	1.3	0.58
G3	6.9	6.8	0.94	0.1	6.1	1.1	0.56
G4	7.1	7.0	0.96	0.1	6.0	1.1	0.59
G5	8.9	8.6	0.97	0.3	8.0	1.2	0.74
G7	6.3	6.2	0.97	0.1	5.1	1.2	0.62
G8	7.6	7.5	1.00	0.1	7.5	1.2	0.51
H1	7.6	7.4	0.96	0.2	6.8	1.2	0.56
H2	8.4	8.0	0.97	0.4	7.7	1.3	0.55
H3	5.4	5.1	0.91	0.3	4.2	0.9	0.64
J1	6.1	6.1	0.87	--	9.2	1.0	0.33
J2	6.3	6.3	0.87	--	8.9	1.0	0.35
J4	7.0	7.0	0.93	--	5.7	1.1	0.61
J5	6.9	6.9	0.93	--	5.6	1.1	0.62
J6	7.6	7.6	0.95	--	5.3	1.6	0.72
J7	7.2	7.1	0.99	0.1	5.8	1.3	0.62
J8	6.5	6.4	0.94	0.1	5.0	1.3	0.65
K1	4.2	4.2	0.67	--	2.6	1.3	0.81
K2	5.3	5.3	0.87	--	4.2	1.3	0.63
K3	6.3	6.3	0.92	--	6.8	1.3	0.46
K5	4.3	4.3	0.74	--	3.2	1.3	0.67
K6	5.4	5.4	0.96	--	4.4	1.2	0.61
K7	6.1	6.1	0.90	--	5.2	1.1	0.59
K8	6.4	6.4	0.95	--	5.6	1.1	0.57
K9	4.6	3.1	0	1.5	2.6	1.8	0.88
K10	5.4	5.4	0.94	--	7.9	0.2	0.34
L1	7.1	7.1	1.00	--	12.2	0.2	0.29
L3	3.5	3.3	0.50	0.2	4.5	0.5	0.39
L4	5.6	5.6	0.95	--	9.0	0.2	0.31
L5	3.6	3.4	0.61	0.2	5.1	0.1	0.35
L6	3.6	3.5	0.70	0.1	7.8	<0.1	0.23
L7	4.8	4.5	0.89	0.3	10.2	<0.1	0.23
L8	5.6	5.2	0.92	0.4	11.2	0.1	0.25

TABLE 6

COMPOSITIONAL* RATIOS OF EIGHT RIPPLE SPIKES NEARBY FLAT AREA COUPLES AS ANALYZED BY EDAX - WELD SAMPLE G5

Spike Flat Area Couple	Ratio, % in Spike/% in Nearby Flat Area					
	Fe	Ni	Al	Si	Mn	Location
1	0.98	0.87	--	2.8	--	Just After $i_p \rightarrow i_b$
2	1.01	0.95	--	1.3	1.4	Just After $i_b \rightarrow i_p$
3	0.98	1.00	--	1.4	1.4	Just After $i_b \rightarrow i_p$
4	1.09	0.74	--	0.8	--	Just Before $i_p \rightarrow i_b$
5	1.02	0.94	--	0.6	--	Just Before $i_p \rightarrow i_b$
6	0.92	0.85	13.1	4.9	--	Just Before $i_b \rightarrow i_p$
7	0.67	0.46	40.0	17.4	--	Just Before $i_b \rightarrow i_p$
8	1.05	0.88	1.9	0.9	--	Midway in t_b

*Nominal alloy composition, in wt.%: Fe-25.9 Ni-0.34 Mn-0.24 Si-0.012 C.

TABLE 7

TIMES OF WAVE ARRIVALS AT THE WELD POOL TRAILING EDGE

AS DETERMINED FROM HIGH SPEED (~1000 FRAMES/SEC) MOTION PICTURES

		Times Between Wave Arrivals, In Seconds.				
		F3	J4	J7	L1	M1
1st t_b	1st Wave*	0.010	0.015	0.015	0.012	0.008
	2nd "	0.023	0.034	0.030	0.028	0.029
	3rd "	0.022	0.032	0.045	0.023	0.023
	4th "	0.021	0.033	0.045	0.022	0.023
	5th "	0.021	--	0.045	0.022	0.023
	6th "	0.022	--	0.045	0.022	0.024
	7th "	--	--	0.045	0.021	0.024
	8th "	--	--	0.046**	0.022	--
2nd t_b	1st Wave*	--	0.014	--	0.012	0.008
	2nd "	--	0.033	--	0.028	0.027
	3rd "	--	0.033	--	0.023	0.023
	4th "	--	0.032	--	0.022	0.024
	5th "	--	--	--	--	0.024
	6th "	--	--	--	--	--

*First wave arrival time after $i_p \rightarrow i_b$ transition.

**Six more waves were measured with 0.045 second intervals. After these the wave amplitude was too small to be visible.

TABLE 8

AVERAGE RATES OF SOLID GROWTH (R_p and R_b)

DURING t_p AND t_b AT THE WELD POOL TRAILING EDGE

AS COMPUTED FROM RIPPLE SPACING MEASUREMENTS

Weld No.	S_p (mm)	S_b (mm)	S_p/S_b	$(R_p)_{Ave}$ ($cm.s^{-1}$)	$(R_b)_{Ave}$ ($cm.s^{-1}$)	R_p/R_b
F1	≤ 0	≥ 0.389	0	≤ 0	0.233	--
F3	0	0.495	0	0	0.296	--
F4	0.030	0.390	0.08	0.091	0.233	0.39
F5	0.161	0.897	0.18	0.096	0.269	0.36
F6	0.395	0.592	0.67	0.297	0.178	1.67
F7	0.079	0.768	0.10	0.118	0.231	0.51
F8	0.097	0.714	0.14	0.194	0.214	0.91
G1	0.054	1.710	0.32	0.032	0.256	0.12
G3	0.320	1.444	0.22	0.192	0.216	0.89
G4	0.418	1.346	0.31	0.250	0.202	1.24
G5	0.396	1.368	0.29	0.237	0.205	1.15
G7	0.423	1.341	0.31	0.253	0.201	1.26
G8	0.415	1.349	0.31	0.248	0.202	1.23
J1	0.008	0.036	0.22	0.200	0.211	0.95
J2	0.018	0.070	0.26	0.225	0.212	1.06
J4	0.078	0.274	0.28	0.236	0.206	1.14
J5	0.164	0.540	0.30	0.245	0.202	1.21
J6	0.378	1.032	0.37	0.284	0.194	1.46
J7	0.536	1.667	0.32	0.258	0.200	1.29
J8	0.134	1.238	0.11	0.161	0.219	0.73

Dwg. 6445A21

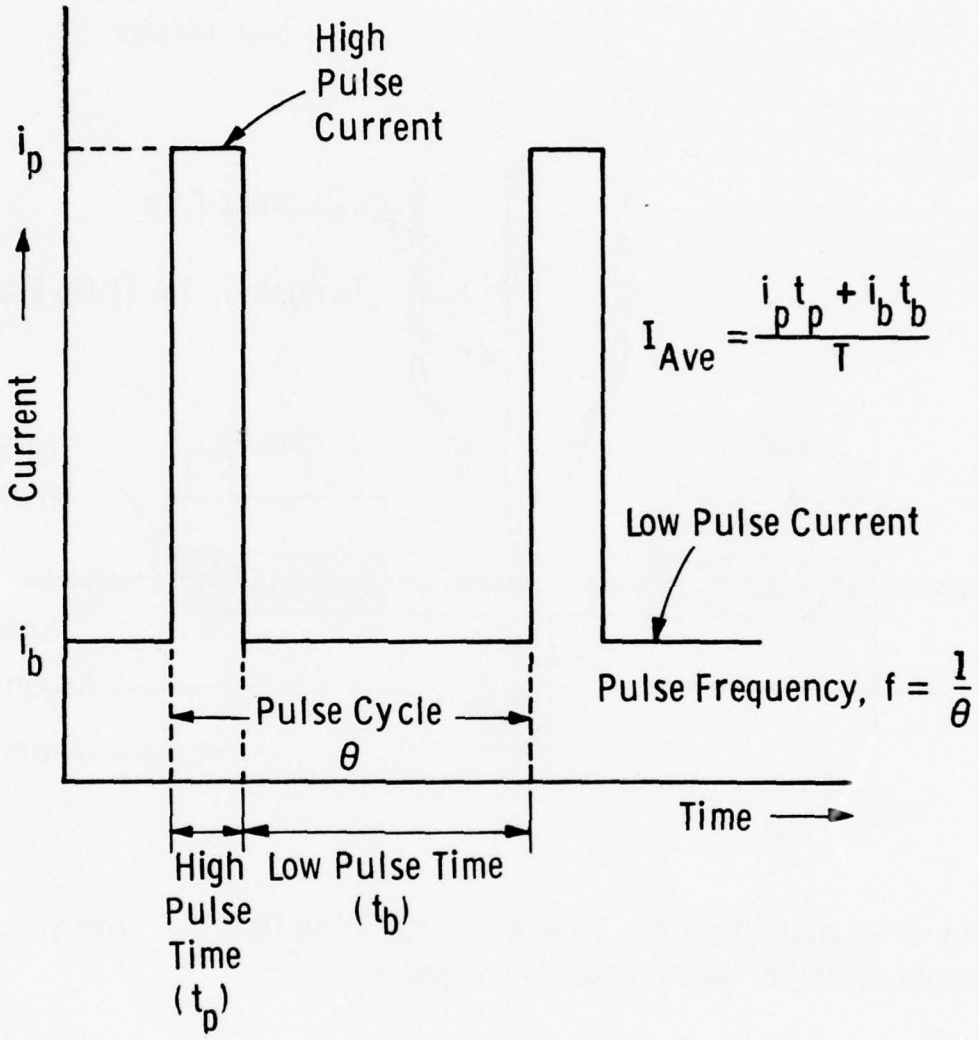

Fig. 1—An idealized pulsed current waveform and associated definitions

Dwg. 6445A22

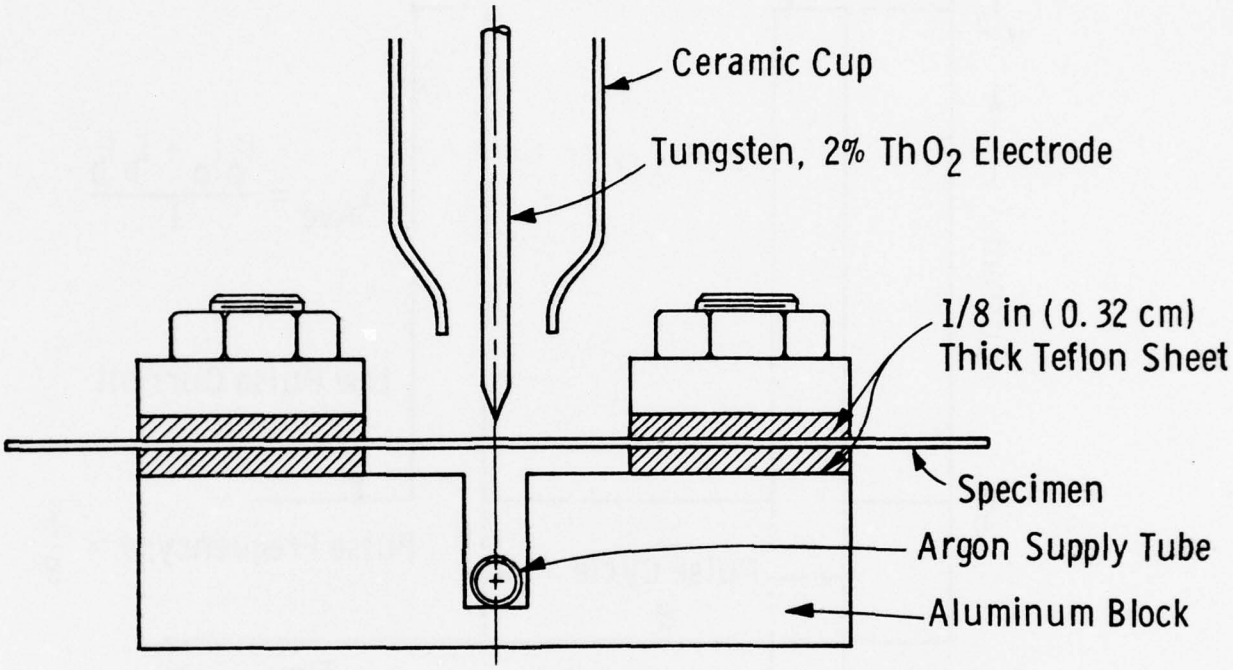

Fig. 2 —Cross-sectional view of the clamping fixture. Torch travel direction was normal to the paper

Dwg. 7710A05

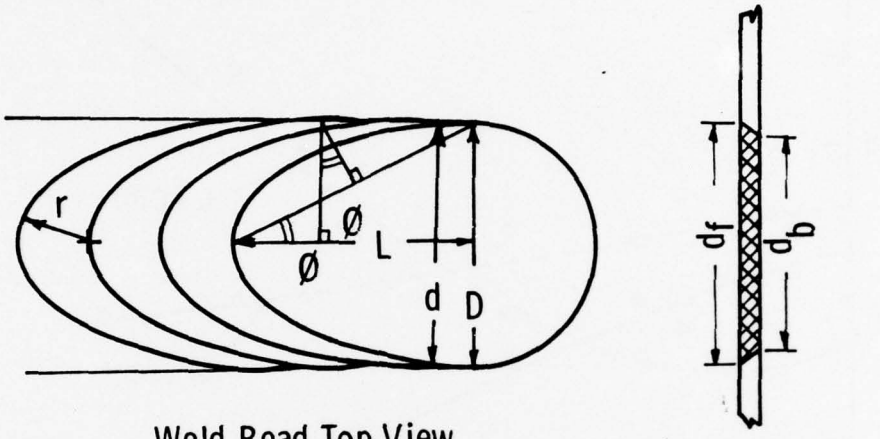

Weld Bead Top View

Cross-Section

Fig. 3 — Definitions related to weld bead and pool shapes

r ---- weld pool trailing edge radius
Ø ---- angle representing grain orientation
L ---- weld pool elongation at its maximum
D ---- the maximum weld bead width
d ---- the minimum weld bead width
d_f ---- average bead width at fron of weldment

$$d_f = \frac{D + d}{2}$$

d_b ---- average bead width at back of weldment

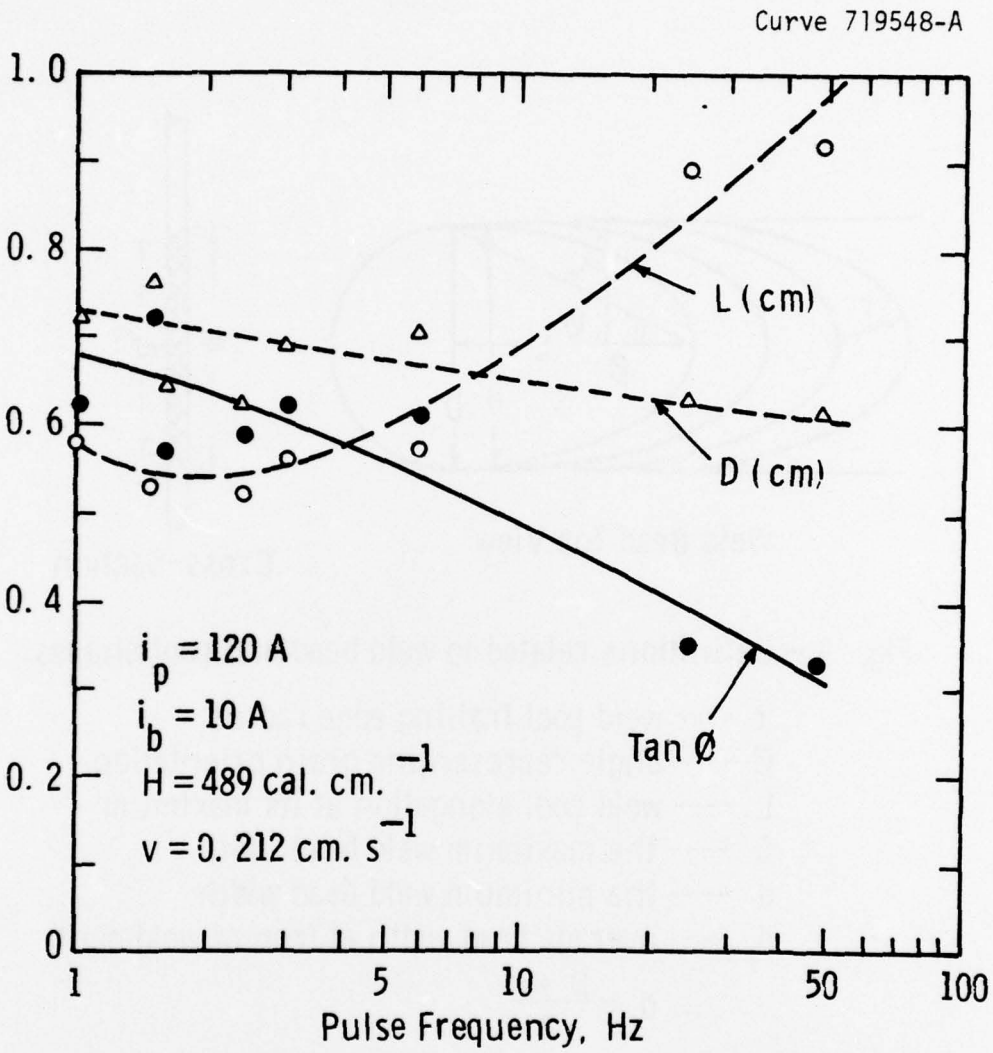

Fig. 4 — Effect of pulsing frequency on weld pool elongation (L), maximum bead width (D), and grain orientation represented by tan Ø (= D/2L).

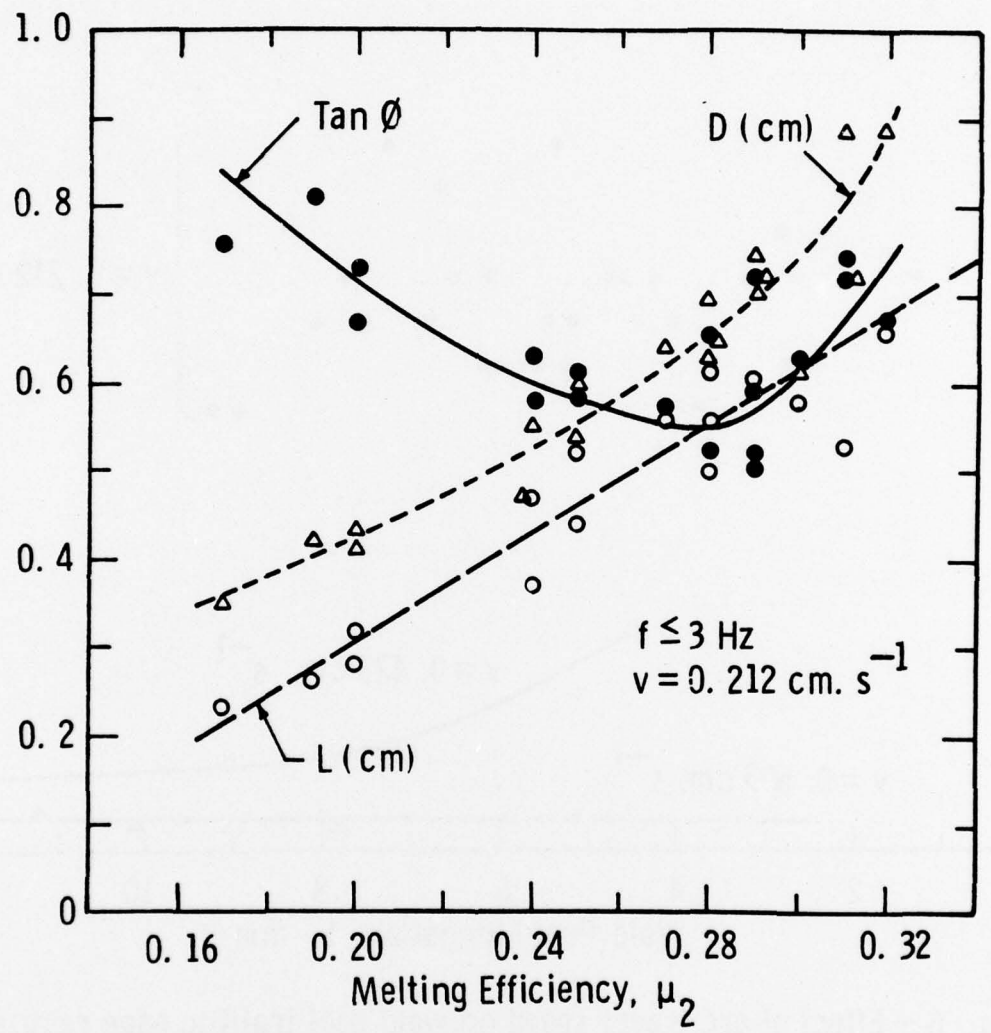

Fig. 5 — Relations between weld pool elongation (L), maximum bead width (D), grain orientation as represented by the angle ($\emptyset = D/2L$), and melting efficiency of the process.

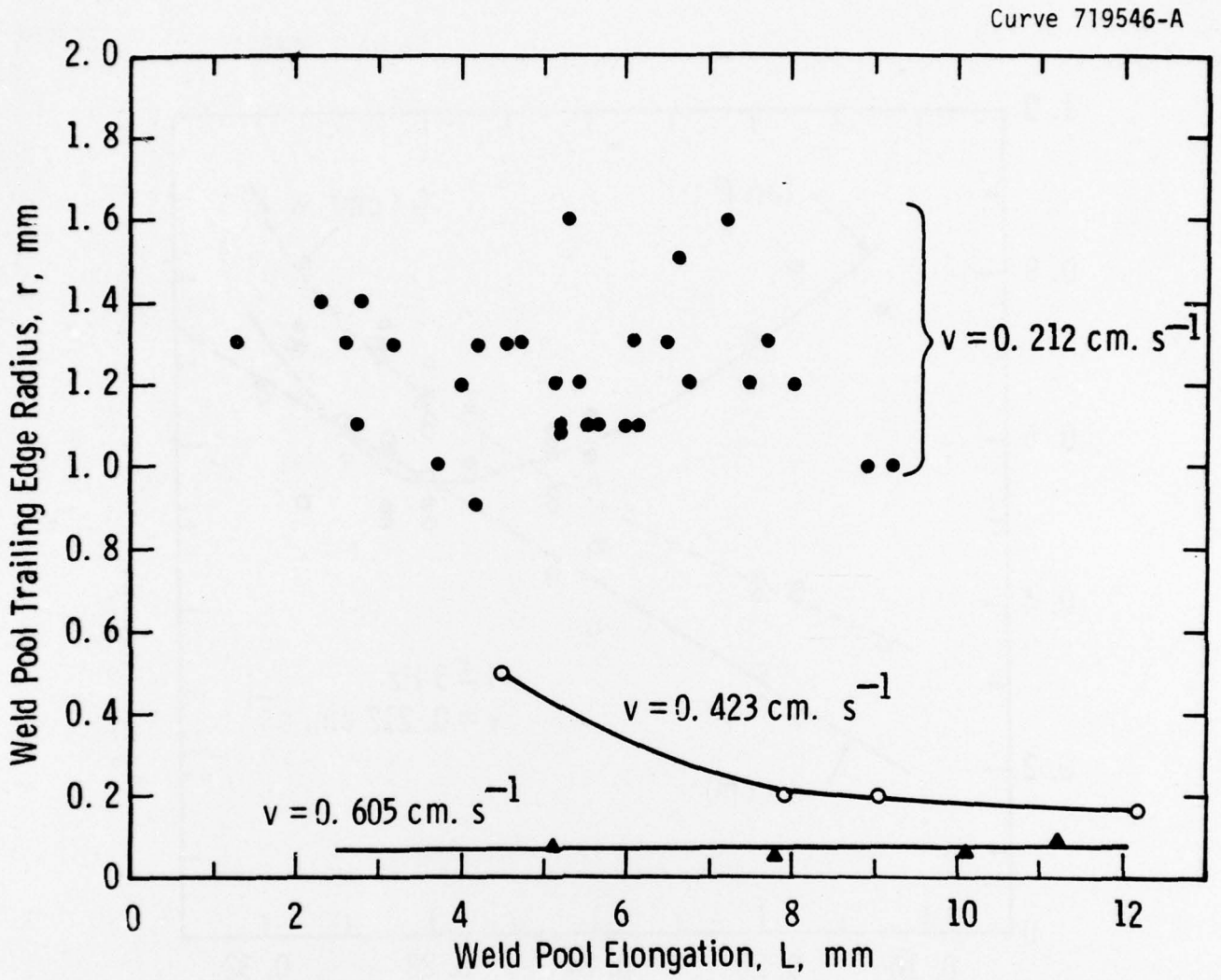

Fig. 6 – Effect of arc travel speed on weld pool trailing edge radius (r) and pool elongation (L).

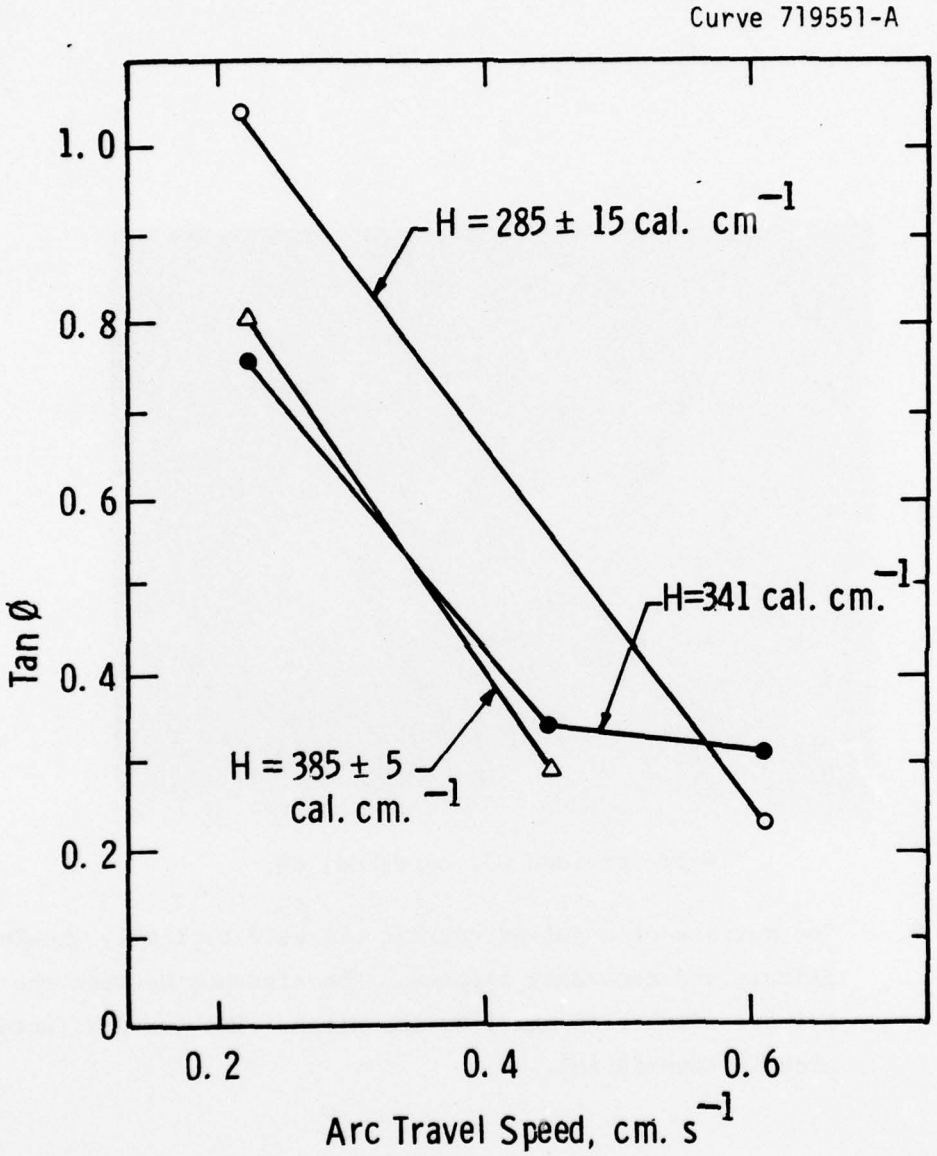

Fig. 7 — Effect of arc travel speed on grain orientation as represented by tan Ø.

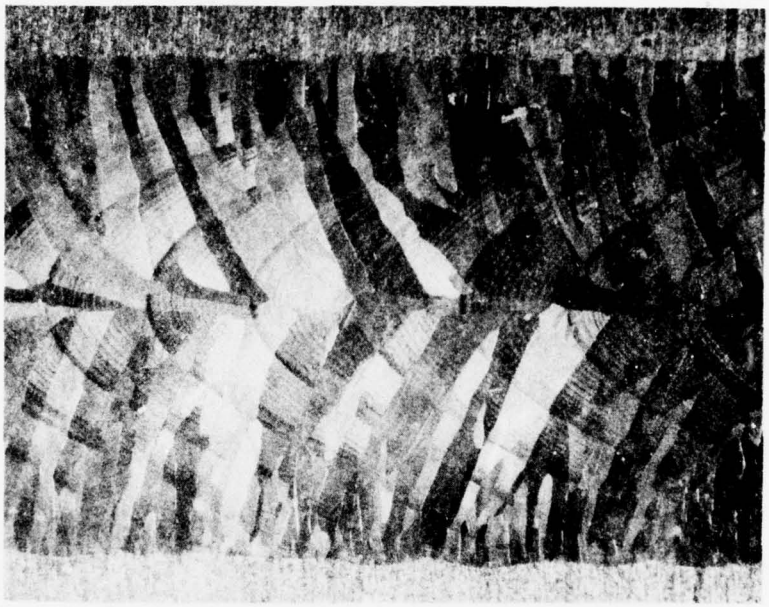

Weld Specimen G5, unetched, 8X.

Figure 8 - Top surface of a pulsed current GTA weld typically showing primary and secondary ripples. The distance between the primary ripples is equal to the pitch. The grain structure seen is superficial.

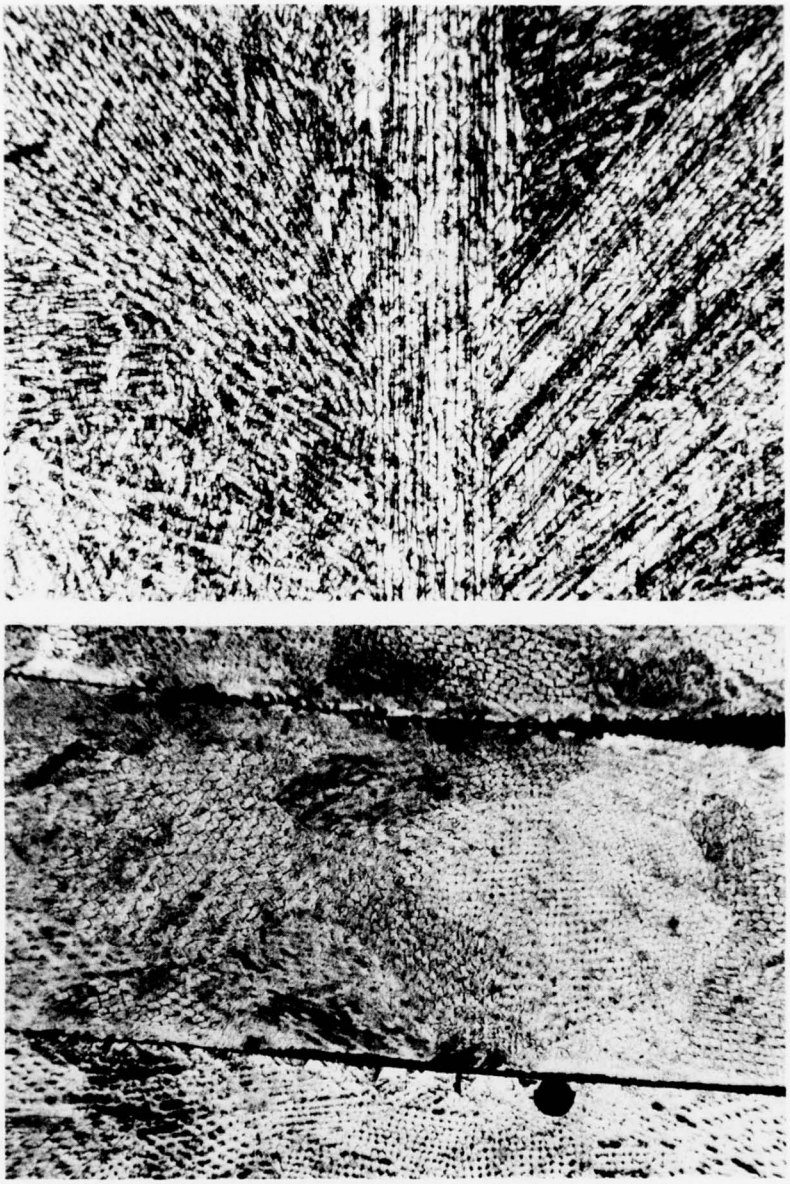

Weld Specimen J4, Marble's Reagent, 55X

Figure 9 - Typical solidification structures of weld No. J4 on planes parallel to the weld surface (top) and transverse to the weld direction (bottom).

One motion picture frame prior to $i_p \rightarrow i_b$ transition.
Note weld ripples previously formed at the bottom portion of the picture.

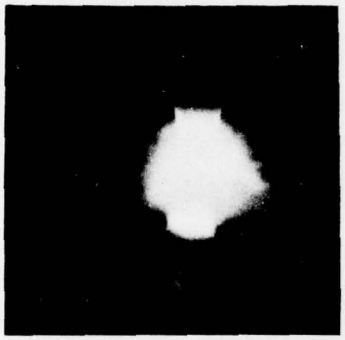

2 frames after $i_p \rightarrow i_b$

7 frames after $i_p \rightarrow i_b$

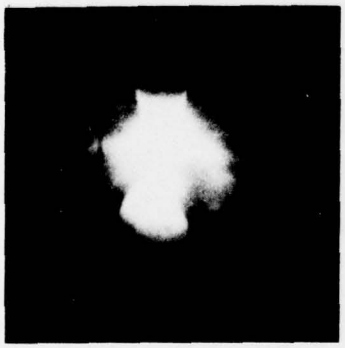

9 frames after $i_p \rightarrow i_b$

11 frames after $i_p \rightarrow i_b$

Figure 10 - A sequence of photos from a high speed (1000 frames/second) movie of weld No. M1 showing the movement of a weld pool wave formed by the transition from a high current arc to a low current arc. Note the electrode tip reflection in the pool move down until it hits the weld trailing edge in the last frame.

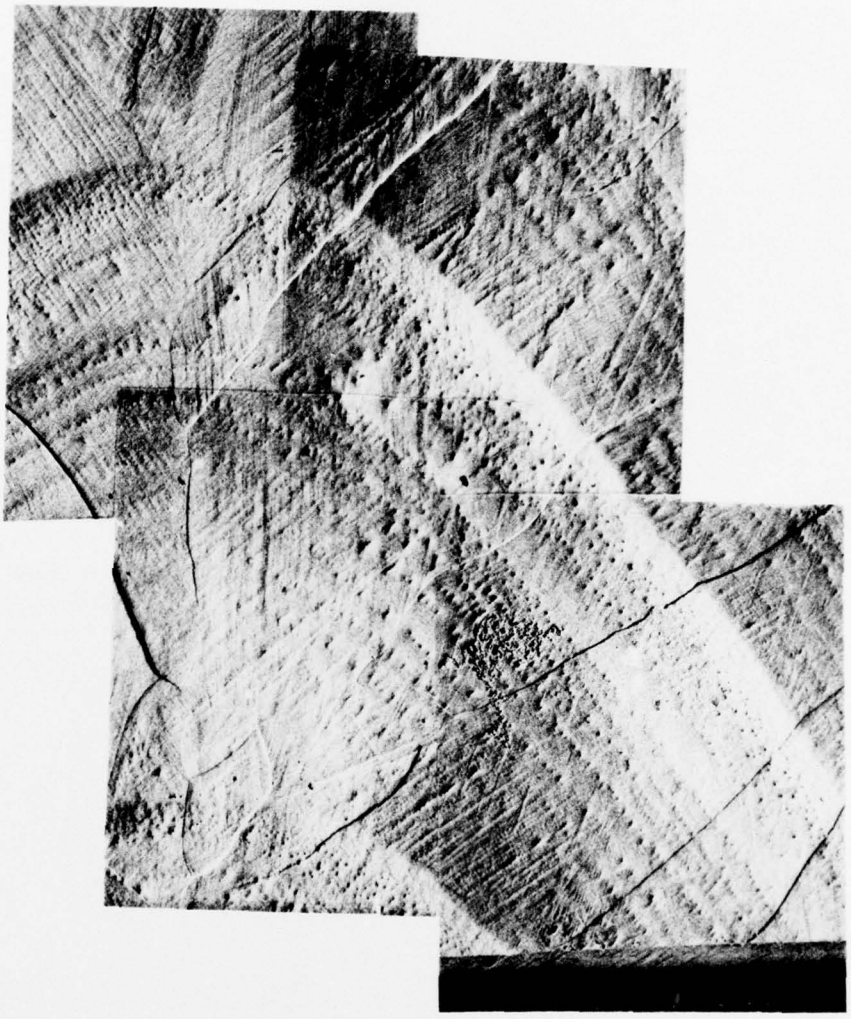

Weld Specimen G5, 52X

Figure 11 - Scanning Electron Microscopic view of the weld metal top surface on as welded Sample G5.

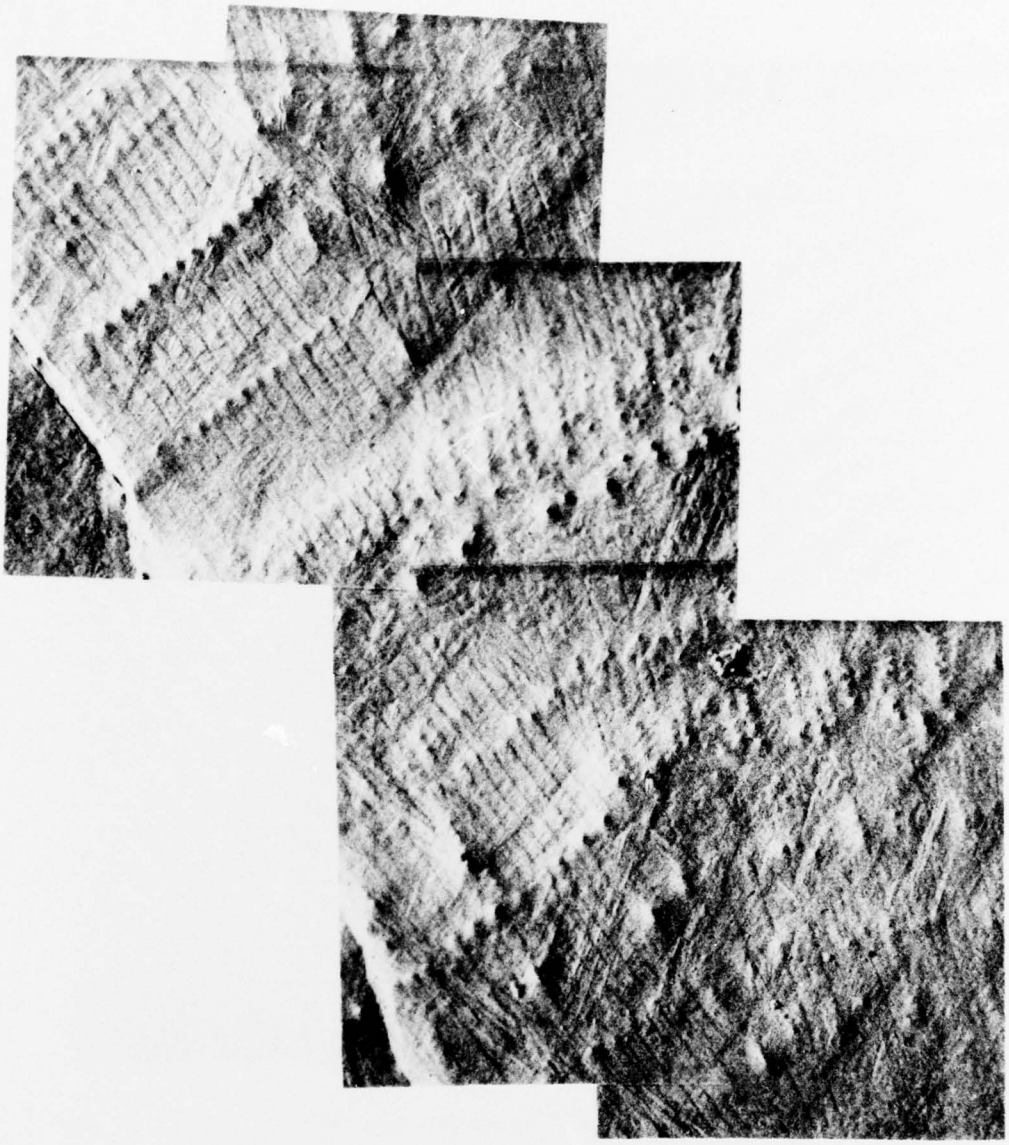

Weld Specimen F3, As Welded Surface, 265X

Figure 12 – A composite of SEM micrographs showing that spikes (constituting a ripple) preferably form at the cell boundaries.

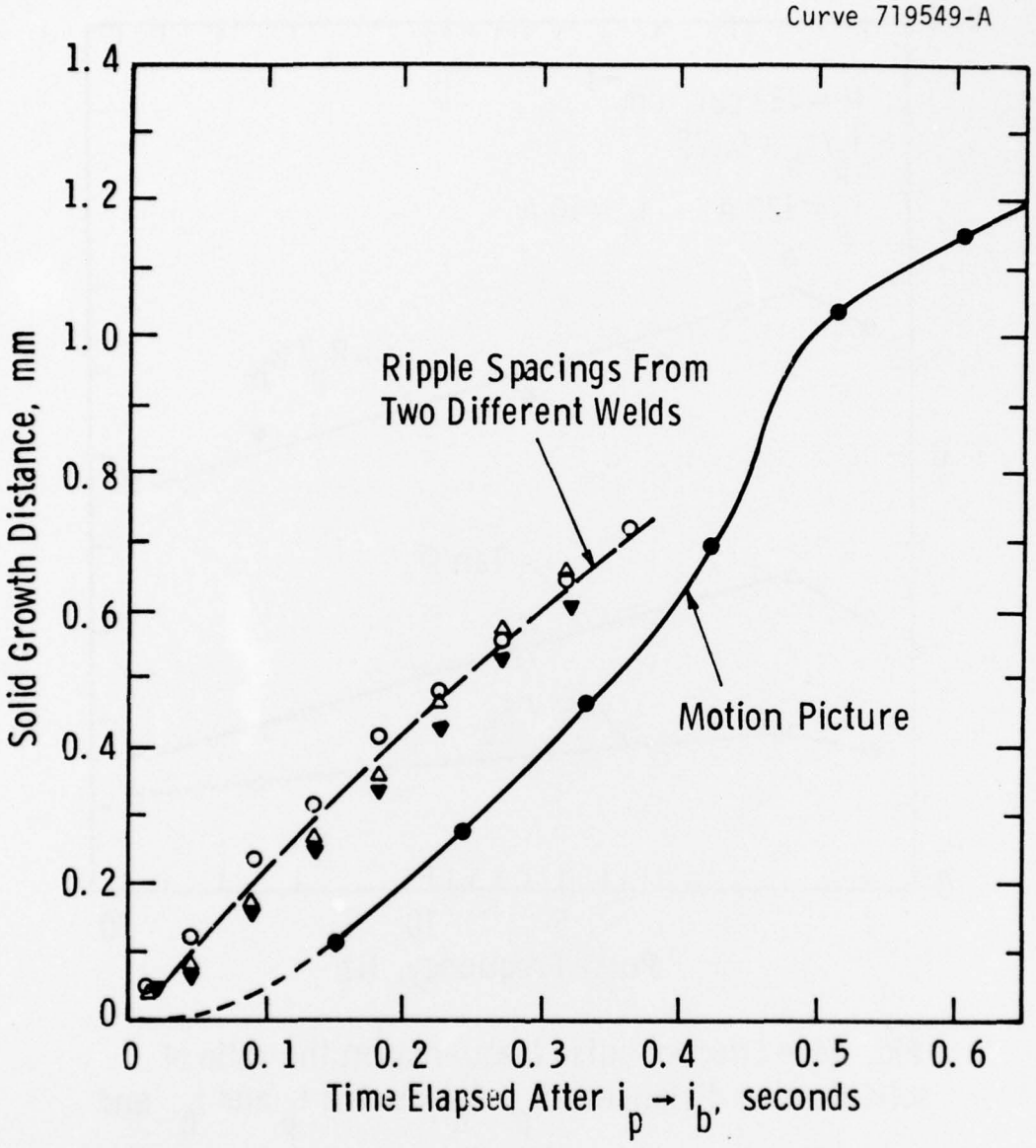

Fig. 13 — A comparison of solid growth at the trailing edge of the weld pool for sample J7 as measured from a high speed motion picture and weld surface ripple spacings.

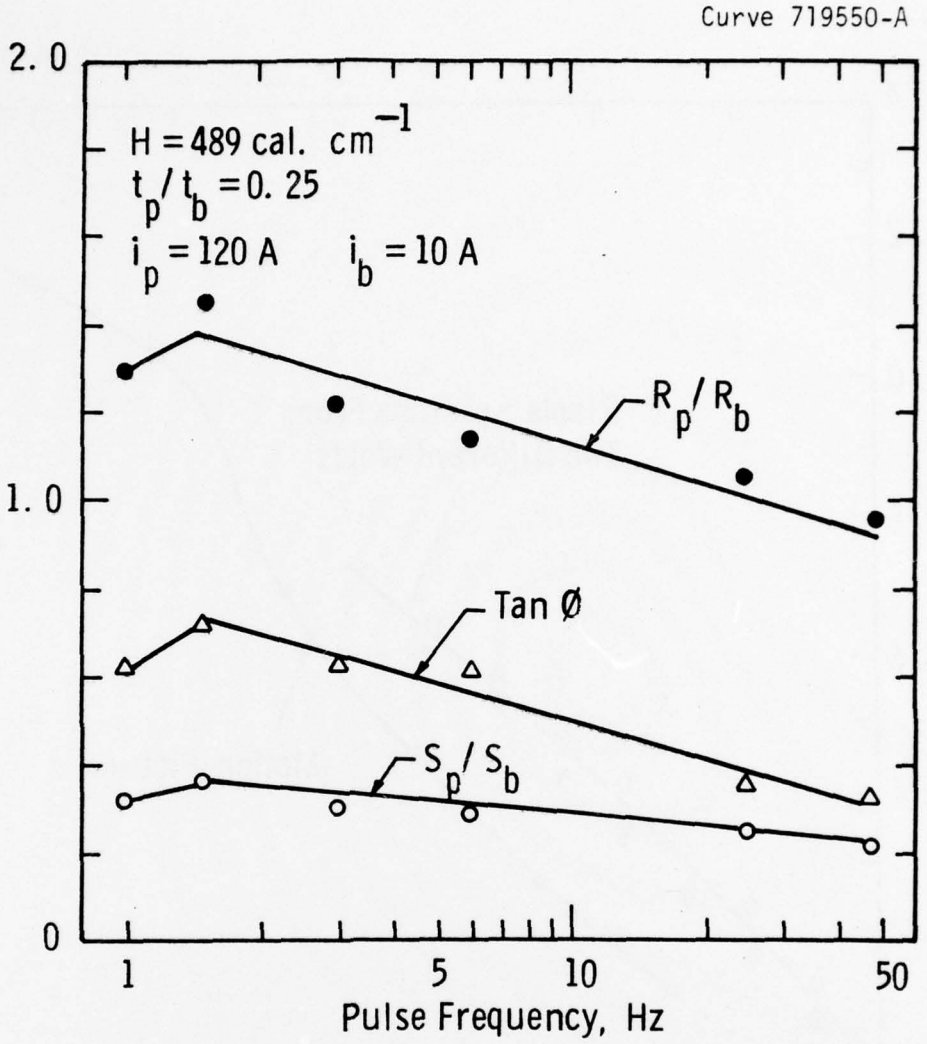

Fig. 14 — Effect of pulse frequency on the ratio of solidification distances (S_p, S_b) during t_p and t_b, and the ratio of rates of solidification (R_p, R_b) during t_p and t_b for the trailing edge of the weld pool. Pulse frequency effect on tan Ø for the same welds is also shown for comparison

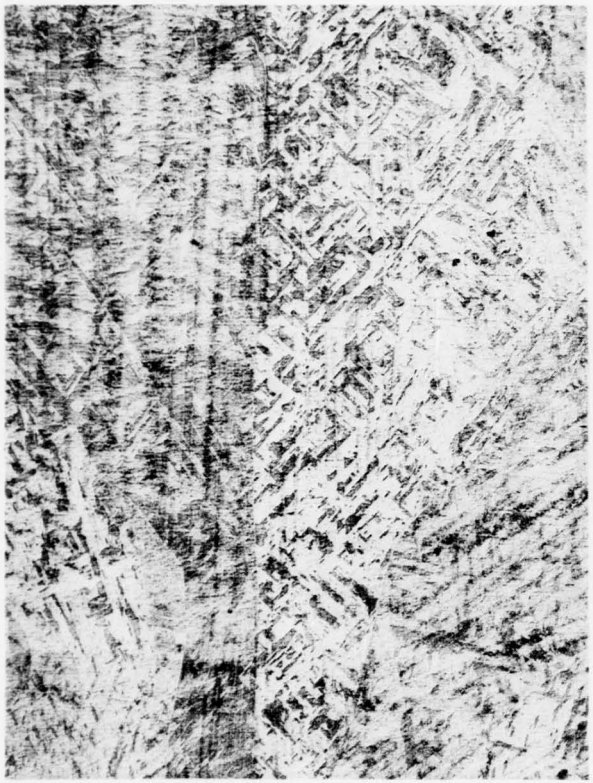

Weld N6, 100X

Weld P6, 100X

Figure 15 - Photomicrographs showing the chilling effect of the thicker plate (right) in the elimination of the continuous centerline grain (left). Marbles Reagent.

Weld Nos.: V4 V3 V2 V1

Figure 16 - A sulfur print of the four welds listed in Table 4. Note the high sulfur concentration near the top of Weld No. V4.